AIAA JOURNAL
Vol. 31, No. 3, March 1993

Aero-Optical Phase Measurements Using Fourier Transform Holographic Interferometry

George Havener* and Denise Kirby†
Arnold Engineering Development Center, Arnold Air Force Base, Tennessee 37389

Arnold Engineering Development Center's current capability to determine optical phase from holographic interferograms using the Fourier transform method is described. Video images of interferograms are digitized into 0–255 grey level intensity arrays nominally 1000 pixels square. One-dimensional discrete Fourier transforms and digital filtering are used to compute the optical phase for each pixel which thereby generates high-resolution phase maps for the interferograms. The phase data are reduced according to the application. For aerodynamic flowfields, density distributions for two-dimensional and axisymmetric flows are obtained and the current capability is applied to an interferogram of Mach 6 airflow over an axisymmetric sharp tip cone at zero angle of attack. For aero-optics testing, statistics such as one- and two-dimensional spatial correlations, integral scales, means, variances, and peak-to-valley rms values for the phase fluctuations are reducible as are calculations for performance parameters such as optical transfer and point spread functions, Strehl losses, and encircled energy diagrams. Current capability is demonstrated by application to interferograms of Mach 8 high Reynolds number airflow between parallel flat plates.

Nomenclature

A	= modulation irradiance, Eq. (1)
B	= offset phase angle, Eq. (1)
C_p	= constant pressure specific heat
$C(x)$	= complex fringe visibility function
$E(x)$	= complex heterodyne frequency function
f	= spatial frequency
f_c	= heterodyne frequency spatial carrier fringes
f_{co}	= cutoff frequency
$H(x)$	= Hamming window-filter function
I	= irradiance
I_0	= background irradiance, Eq. (1)
Im( )	= imaginary part of complex number
j	= imaginary number
K_{GD}	= specific refractivity: Gladstone-Dale constant
k	= wave number, $2\pi/\lambda$
L	= width of two-dimensional flowfield, Eq. (11)
LN	= integer exponent on 2 defining n
$\ell n_c( )$	= complex natural logarithm
mod( )	= modulus of complex number
NINT( )	= nearest integer
n	= number of pixels in y scan, 2^{LN}
n_f	= number of digital filter coefficients, ≥ 40
$R(x_c)$	= extent of axisymmetric field at x_c, Eq. (12)
Re( )	= real part of complex number
r	= radial coordinate, Eq. (12)
T	= temperature
u	= mean velocity
$w(x)$	= Hanning window, $1 - \cos(2\pi \times /n)$
x, y, z	= rectangular coordinates
x_c	= yz plane normal to x
y_c	= y scan, Fig. 1a
$\delta( )$	= delta function
θ	= conical flow angle
λ	= wavelength
μ	= average value
ρ	= density
ϕ	= phase with respect to f_c, Eq. (1)
*	= convolution
{ }	= Fourier transform of

Subscripts

c	= constant value
0	= stagnation state
ρ	= based on density

Superscripts

-1	= inverse
*	= complex conjugate
$'$	= fluctuation quantity
$\hat{}$	= Fourier transformed quantity

Introduction

INTERFEROMETRY has long been useful for obtaining optical measurements of aerodynamic flowfields, and holographic techniques[1] have provided numerous methods whereby interferometry can be applied proficiently to many types of gas dynamic investigations. While interferometric flow visualizations are always informative, the primary benefit lies in the opportunity to obtain quantitative information, specifically flowfield density or statistics that define levels of wave front distortion.

The first step in reducing an interferogram is determination of the optical phase map. The optical phase map is the unique quantified description of the changes in the optical path lengths visually seen in the interferogram; and, until recently, fringe tracking techniques were used in this first step. Regardless of the special features of the fringe tracking algorithms, human interfacing was required which made these techniques time consuming, costly, and prone to error. Semiautomated fringe tracking processes preceded the current phase demodulation techniques, but these were also less than satisfactory, as the tracking algorithms failed at points where "fringe break ups" or "fringe islands" occurred. Today, automated phase demodulation techniques allow interferogram reduction to be done quickly and efficiently. Depending on the application, the amount of data obtained from a single interferogram is typically 10–100 times more, and resolutions approaching $\lambda/100$ are realistic.

Presented as Paper 92-0379 at the AIAA 30th Aerospace Sciences Meeting, Reno, NV, Jan. 6–9, 1992; received March 2, 1992; revision received May 22, 1992; accepted for publication June 5, 1992.

*Principal Engineer, Calspan Corporation/AEDC Operations. Associate Fellow AIAA.

†Scientific Computer Programmer, Calspan Corporation/AEDC Operations.

Phase demodulation involves computation of optical phase directly from discrete quantification for the variation in the irradiance defined in an interferogram. The basic process is illustrated in Fig. 1. The x distribution for the irradiance along y_c is

$$I_{(x)} = I_0(x) + A(x)\cos[2\pi f_c x + \phi(x) + B] \tag{1}$$

Currently, three phase demodulation techniques in use or refinement are 1) heterodyne interferometry,[2] 2) phase-shift interferometry (PSI),[3] and 3) the Fourier transform method[4] herein referred to as Fourier transform interferometry (FTI).

With regard to FTI, in 1982 Takeda et al.[4] presented a description and demonstration for a one-dimensional discrete Fourier transform fringe reduction algorithm as well as a method for phase unwrapping. The following year, Macy[5] described an algorithm to resolve two-dimensional phase fields, reviewed the technique of Takeda and the sinusoidal curve fitting method of Mertz,[6] and presented a discussion on error sources. Later, Nugent[7] offered a synopsis on the Takeda method and discussed errors attributable to data sampling and film nonlinearities. In 1987, Roddier and Roddier[8] presented a discussion on specific error contributions for the terms in Eq. (1), and a reference that traces the apparent origin of the Fourier transform method to their work in 1976. A method for using two different Fourier transform intensities,[9] a method using iterative Fourier transforms,[10] and a good discussion on general problems and approaches[11] are recent publications.

Arnold Engineering Development Center (AEDC) has recently installed FTI to support testing requirements at the Center, and two initial applications have been done to demonstrate utility. One pertains to the measurement of density for Mach 6 high Reynolds number airflow over a sharp tip cone at zero angle of attack,[12,13] and the other pertains to measurement of aero-optical wave front distortions for Mach 8 high Reynolds number airflow between parallel flat plates in the AEDC hypersonic tunnel C.[14,15] The details of the AEDC capability and the preliminary results of the applications are presented here.

Fourier Transform Interferometry

With respect to Fig. 1, the discrete Fourier transform (DFT) {Eq. (1)} is used to obtain the spatial power spectrum illustrated in Fig. 1b. As the spatial variations of I_0, A, and ϕ are usually small compared to f_c, the power spectrum is trimodal consisting of an $\hat{I}_0(f)$ band centered on the origin and two sidebands for the sinusoidal modulation which are located to the right and left of the origin by $\pm f_c$, respectively. The spatial fringe distribution defined by f_c is removed by translating the spectrum laterally so that either the right or left sideband is centered on the origin. Then a digital lowpass filter is used to save the newly centered sideband, and an inverse discrete Fourier transform is used to recover the filtered data from the frequency domain. As shown in the following, these data uniquely contain the phase information.

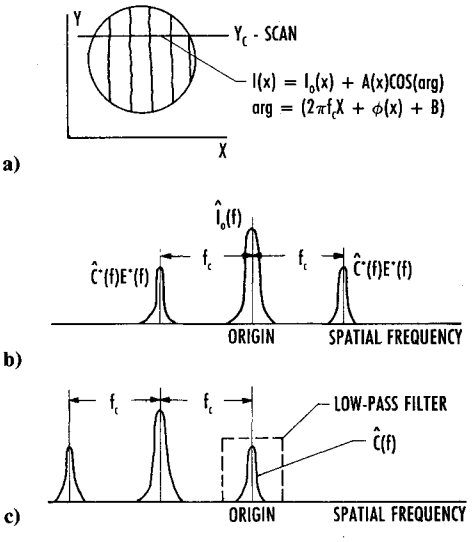

Fig. 1 Principles of the Fourier transform method: a) irradiance distribution, b) power spectrum for $\hat{I}(f)$, and c) power spectrum for $\hat{I}(f-f_c)$.

The key mathematical steps are shown next. First, Eq. (1) is written in exponential form

$$\begin{aligned} I(x) &= I_0(x) + \frac{A}{2}\exp\left(j[2\pi f_c x + \phi(x)]\right) \\ &\quad + \frac{A}{2}\exp(-j[2\pi f_c x + \phi(x)]) \\ &= I_0(x) + C(x)E(x) + C^*(x)E^*(x) \end{aligned} \tag{2}$$

with

$$C(x) = \frac{A}{2}e^{j\phi(x)} \qquad E(x) = e^{j2\pi f_c}$$

Isolation of $C(x)$ is the objective of phase demodulation. $E(x)$, also a complex function with a real part defined by f_c, is used to produce proper translation of $\hat{I}(f)$ which is done here by multiplying Eq. (1) by $E^*(x)$ to obtain

$$I(x)E^*(x) = C(x) + I_0(x)E^*(x) + C^*(x)(E^*(x))^2 \tag{3}$$

after which, the DFT of {Eq. (3)} gives

$$\hat{I}(f-f_c) = C(f) + \hat{I}_0(f-f_c) + \hat{C}^*(f-2f_c) \tag{4}$$

with $\hat{C}(f)$ now distinct at the origin as shown in Fig. 1c. Note that the DFT of {Eq. (2)} defines a spectrum with $\hat{I}_0(f)$ centered at the origin (Fig. 1b). The convolution, $\hat{I}(f)*E^*(f)$, shifts the spectrum to $-f_c$ thereby leaving $\hat{C}(f)$ centered at the origin. The convolution theorem[16] forms the Fourier transform pair

$$\hat{I}(f)*\hat{E}^*(f) = \mathrm{DFT}\{I(x)E^*(x)\} \tag{5}$$

with

$$\hat{E}^*(f) = \hat{\delta}(f+f_c) \quad \begin{matrix} = 1, f = -f_c \\ = 0, \text{elsewhere} \end{matrix}$$

Use of a lowpass digital filter followed by the DFT^{-1} of $\{C(f)\}$ completes the isolation of $C(x)$; the remaining data in Eq. (4) are discarded since $C(x)$ uniquely contains the phase data. Specifically,

$$\begin{aligned} \phi(x) &= \mathrm{Im}[\ell n_c(C(x))] \\ A(x) &= 2\exp\left(\mathrm{Re}[\ell n_c(C(x))]\right) \end{aligned} \tag{6}$$

Some comments are worthwhile. First, the convolution $\hat{I}(f)*\hat{E}^*(f)$ is done correctly only when f_c is rational. When f_c is irrational, the DFT $\{E^*(x)\} \neq \hat{\delta}(f+f_c)$. As illustrated in Fig. 2, the power spectrum for $\hat{E}^*(f)$ with f_c irrational is a band, not a delta function, and the convolution now corrupts the data in $I(x)$ which places errors in $\phi(x)$.

Second, $\hat{C}(f)$ and $\hat{I}_0(f-f_c)$ must be band limited and enough separated so that frequency aliasing does not occur (no band overlaps, as illustrated in Fig. 3). Construction of the digital lowpass filter requires definition of a cutoff frequency f_{co}, which is done heuristically as only its purpose is well defined; f_{co} must be large enough so that the filter completely and uniquely isolates $\hat{C}(f)$, but not so large that frequencies from $\hat{I}_0(f-f_c)$ are included. For aliased data, f_{co} does not

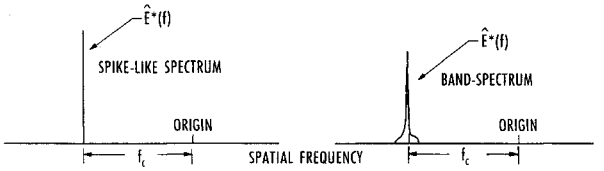

Fig. 2 Illustration showing correct and incorrect $E^*(f)$ spectra: a) correct, rational f_c and b) incorrect, irrational f_c.

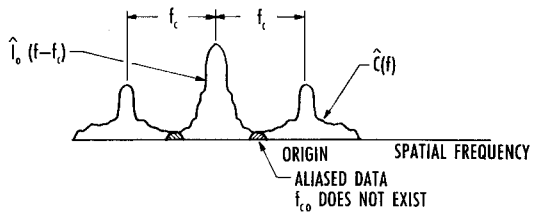

Fig. 3 Illustration of frequency aliased data.

exist and FTI fails. Increasing f_c may eliminate the aliasing, but if not, an alternative method such as PSI is needed.

Third, filtering Eq. (5) removes only the component of f_c that in a vector sense points in the x direction. For askew spatial carrier fringes, the plane of tilt for the interference is not about the y axis, and a residual component of f_c remains in $\phi(x)$. The f_c fringes are caused by angular displacement between the interfering light waves which for collimated waves are seen as uniformly spaced parallel fringes because the continuous phase distribution is defined by a tilted plane. Hence, these fringes are often called "tilt fringes." When the tilt is askew (not about x or y alone), the fringes are slanted with respect to an x, y orthogonal coordinate system. Bone et al.[17] describe a method for removing the heterodyne fringes in the space domain instead of in the frequency domain. They use a section of the interferogram where the fringes are known to be undisturbed, compute the slope of the tilt plane for this section (the slope is the number of pixels per fringe), and then with f_c equal to the reciprocal of the slope, remove f_c from $\phi(x, y)$; they also describe methods for coping with errors caused by edge effects, discuss sampling requirements needed to avoid aliasing, and describe estimates for two-dimensional band limits.

Phase Unwrapping

The periodicity of the sinusoidal modulation in Eq. (1) causes $\phi(x)$ to be initially bound to modulo-2π. The phase angles are said to be wrapped because the principal values are returned on $[-\pi, \pi]$. Phase unwrapping is necessary to reduce flowfield interferograms containing phase shifts greater than 2π, because flow density must be computed from continuous phase data. However, since $\phi(x, y)$ from all interferograms will likely contain erroneous 2π phase jumps caused by edge effects or background noise, phase unwrapping is also needed to validate the data and to identify localities of errant phase information.

Figure 4 illustrates the problem. Figure 4a illustrates fictitious $\phi(x)$ where the phase angles increase steadily toward π. Eventually continuous phase angles greater than π are computed, and since these angles are outside $[-\pi, \pi]$, automatic wraparound returns them with -2π added. Wraparound continues until another 2π jump is encountered, or until once again the computed phase angles are naturally in $[-\pi, \pi]$. For Fig. 4, unwrapping is simple; 2π are added to $\phi(x)$ pixels 10–20 to obtain the continuous distribution illustrated in Fig. 4b. In other cases, more robust methods may be needed.

As with FTI, Ref. 4 appears to be the first reporting of a phase unwrapping algorithm. Nugent[7] and Bone et al.[17] also discuss methods which they found useful. Huntley's[18] noise-immune algorithm relies on the fact that the phase change between two points in an interferogram (two pixels in the digital image) is constant regardless of the path followed in moving from one pixel to another. When this condition is violated, a singularity is identified (Huntley calls them discontinuity sources), and fictitious cut lines connecting the singularities are used to bound the irregularities. A concern for this algorithm is that it may be inappropriate at shock waves and shock-shock interactions where large density gradients may generate effective phase discontinuities, but this point needs further study. Haniff[19] writes about a technique using a nonlinear least-squares algorithm that fits "Fourier phases directly to modulo-2π measurements . . . , thus eliminating the need for phase unwrapping," and Bone[20] has recently presented an elaboration on Huntley's[18] method with improvements using what he calls a mask algorithm and a flood unwrap algorithm.

Fourier Transform Interferometry at Arnold Engineering Development Center

In the AEDC system (Fig. 5), the light waves diffracted from the holograms are used to form interferograms which are then converted directly into digital images using either a 500 line or a 1000 line high-resolution video camera matched to a high-resolution image processor. Pixel definition is made by dividing the camera scan lines into digital increments to obtain rectangular data arrays of 480×512 or 1009×1024 (rows $\times$ columns); the columns are 2^{LN} for the DFT computations ($LN = 9$ or 10 here). Light intensities are quantified by integer gray levels [0, 255] for each pixel. To minimize error from low-frequency electronic noise and optical background noise, each interferogram image is recorded and digitized 16 times, averaged, and then stored on hard disk.

Heterodyne Fringes

For stationary heterodyne fringes, the fringe orientation is fixed with a distribution given by f_c. For digital interferograms, f_c is the number of pixels along y_c corresponding to a change in optical path length between the reference and rotated optical wave fronts. Numerically, f_c is the inverse of the number of pixels between adjacent fringe centers. Determining f_c is a crucial step in FTI, and when f_c is unknown a priori, as is generally the case, sometimes it can be determined directly from the interferogram. As $\hat{I}(f)$ is trimodal, f_c is seen in the power spectrum as the change in the frequency between the origin and the peak of either sideband (Fig. 1b). Thus by computing the average power spectrum for several y_c in a

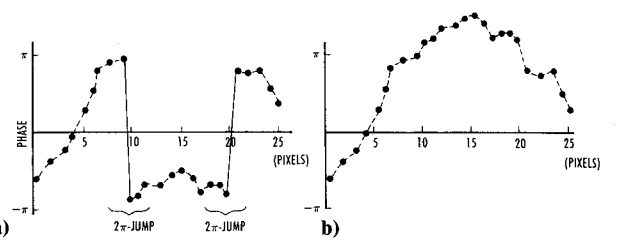

Fig. 4 Illustration of wrapped and unwrapped phase data: a) discontinuous $\phi(x, y_c)$ and b) continuous $\phi(x, y_c)$.

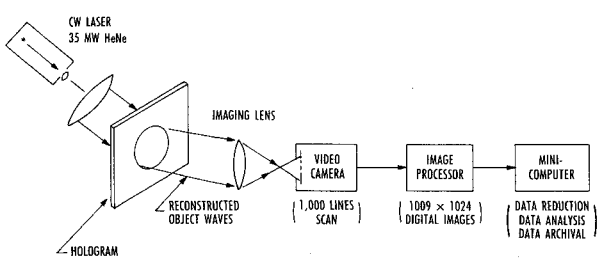

Fig. 5 AEDC hologram playback system for FTI data reduction.

section of the interferogram where the carrier fringes are uniquely defined, f_c is identifiable.

The section of the interferogram used to determine f_c should contain spatial carrier fringes that are straight, uniformly spaced and parallel. In aerodynamic flowfield applications, the spectra must be computed for sections where the flow is known to have no density gradients, upstream of shock waves, for example. In wave front distortion testing of aero-optical flows, determining f_c from the interferogram can be difficult especially if no sections are known to have pure f_c fringes. And for interfering spherical waves, the tilt plane does not exist; here the fringes have continuous curvature and are nonuniformly spaced because the optical interference occurs along curved surfaces mathematically given by hyperbolas. Some experiences[14,15] have shown that if departure from truly pure f_c fringes is small for specific sections of otherwise imperfect interferograms, a good approximation for f_c can be found and FTI can be used to resolve the phase for those sections. Otherwise f_c has to be determined independently, for example, by using hardware to preset f_c for each subsequent interferogram.

Filter Construction

The lowpass digital filter is a Hamming window,[21] the extent of which depends on f_{co} which is arbitrarily set here to be 40% of f_c. The number of terms in the filter is

$$n_f = \text{NINT}\ (2/f_{co})$$

The filter is a digital array, $H(x)$, with real coefficients computed from

$$H(x) = 2.0\, f_{co}[0.54 + 0.46 \cos\ (\pi x/n_f)]\ \frac{\sin(2\pi f_{co}x)}{2\pi f_{co}x} \qquad (7)$$

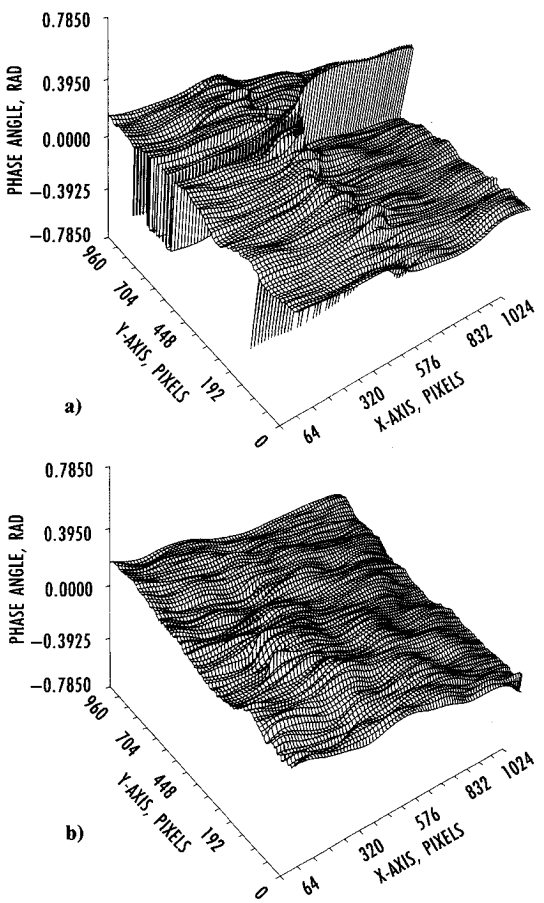

Fig. 6 Exhibit of 2π errors in demodulated phase data: a) wrapped phase map, and b) unwrapped phase map.

Demodulation

Filtering is the convolution of the intensity data and the digital filter function which via the convolution theorem, is

$$\text{DFT}\{I(x)*H(x)\} = \hat{I}(f-f_c)\ H(f) \qquad (8)$$

The digital values for $H(x)$ are computed according to Eq. (7), and $H(f)$ is obtained from the DFT $\{H(x)\}$. Next $E^*(x)$ is computed according to Eq. (2), multiplied against $I(x)$ according to Eq. (3), and the DFT is computed according to Eq. (4). Filtering is done as per the right-hand side of Eq. (8) which annihilates $\hat{I}(f-f_c)$ except for $C(f)$, and Eq. (6) is used to obtain $\phi(x)$. Repetition of this process for all y_c completes the demodulation of $\phi(x, y)$ from $I(x, y)$.

Verification

The $\phi(x, y)$ data are verified by generating an ideal interferogram based on values computed from Eq. (6), and also by plotting a three-dimensional phase map. In an ideal interferogram, I_0 and A are constants and fringe bending results solely from variations in $\phi(x, y)$. Thus by arbitrarily setting $I_0(x) = A(x) = 125$ and $B = 0$, Eq. (1) and $\phi(x, y)$ are used to compute gray level intensities for a verification interferogram, and an image processor is used to display the results. When the $\phi(x, y)$ data are correct, the fringes in the real and verification interferograms are congruent, and likewise, they are incongruent whenever $\phi(x, y)$ is wrong. However, fringe congruency is insufficient verification, because the periodicity of the modulation term in Eq. (1) prevents identifying errant 2π phase jumps, so another check on $\phi(x, y)$ is needed.

Graphical construction of a three-dimensional phase map which shows the location of all 2π phase jumps is the other check performed in the AEDC system. The three-dimensional phase map also reveals the wrapped phase values which appear as discrete steps; Fig. 6 shows wrapped (Fig. 6a) and unwrapped (Fig. 6b) phase maps for the same $\phi(x, y)$ data obtained from the interferogram shown in Fig. 11. Used together, these verification procedures allow the $\phi(x, y)$ data to be corrected before further reductions are made.

Aerodynamic Flowfield Demonstration

Mass density is computed from phase maps reduced from interferograms of Mach 6 airflow over a sharp tip cone at zero angle of attack.[12,13] Figure 7 shows a finite fringe interferogram and the analysis window used for the FTI demonstration (Fig. 7a), a digitized image of the analysis window (Fig. 7b), and the corresponding verification interferogram (Fig. 7c). The numbers above the fringes are general identifiers. The apparent congruency of interferograms Figs. 7a and 7c is a qualitative measure of the accuracy of $\phi(x, y)$ which for this case is good. Figure 8a shows the wrapped phase data for the vertical A-A section line shown in Fig. 7a, and Figs. 8b and 8c show the unwrapped phase along A-A and the three-dimensional phase map for the full window, respectively.

Axisymmetric flow densities for section A-A are compared to the inviscid flow prediction in Fig. 9. For axisymmetric flows, the density is obtained from the inversion of

$$\phi(x_c, y) = kK_{GD}\int_y^R \frac{\rho(r) - \rho_{ref}}{\sqrt{r^2 - y^2}}\, 2r\, dr \qquad (9)$$

Here x points in the flow direction, y is vertical, z points in the direction of light wave propagation, r is radial coordinate with respect to the cone axis, and ρ_{ref} is the density of the freestream air. Equation (9) is transformable to an Abel integral after which different inversion schemes can be used to determine $\rho(r)$ (Ref. 12). Recently, Smith et al.[22] and Kalal and Nugent[23] developed Abel inversion algorithms using Fourier transforms; and Mao et al.[24] demonstrated the method described by Kalal and Nugent on interferograms of

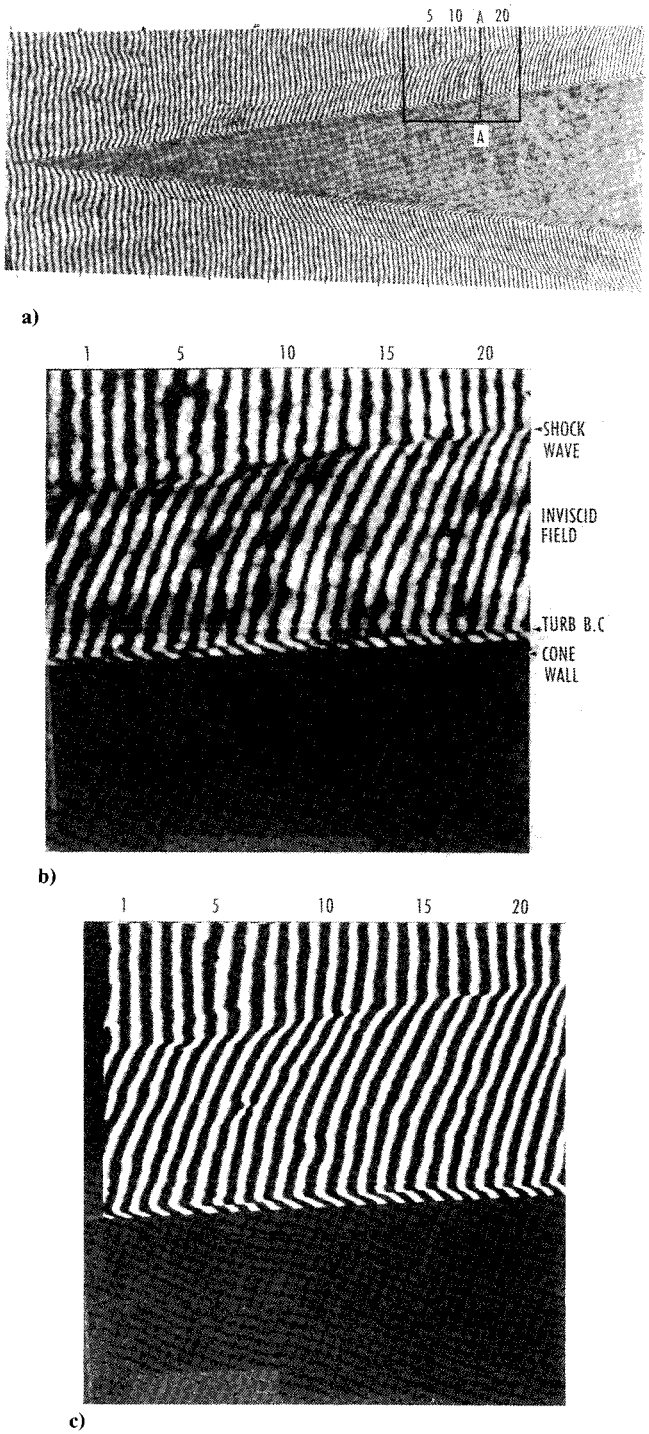

Fig. 7 FTI reduction of $M = 6$ airflow over a sharp tip axisymmetric cone: a) holographic interferogram, b) digitized interferogram, and c) verification interferogram.

an axisymmetric reacting flow. For this demonstration, the delayed differentiation method[12] and a Fourier transform method[24] are used to compute the inviscid flow densities; results for the boundary layer are not included now. Although both techniques give acceptable results, the Fourier transform method appears to be less affected by local phase irregularities. If the interferogram were a measure of truly inviscid flow with no turbulence, both methods would likely produce results close to inviscid-flow cone theory. But the flow is turbulent and these interferograms are instantaneous measurements of the flow unsteadiness. The 20-ns exposure of the pulse ruby recording laser is at least two orders of magnitude smaller than the nominal period of the turbulence time scale,[13] and thus density distributions depart from steady inviscid flow predictions.

Noteworthy here, the phase map in Fig. 8c is based on approximately 200,000 pixels, a data sampling for global flowfield measurements unheralded by nonoptical measurement

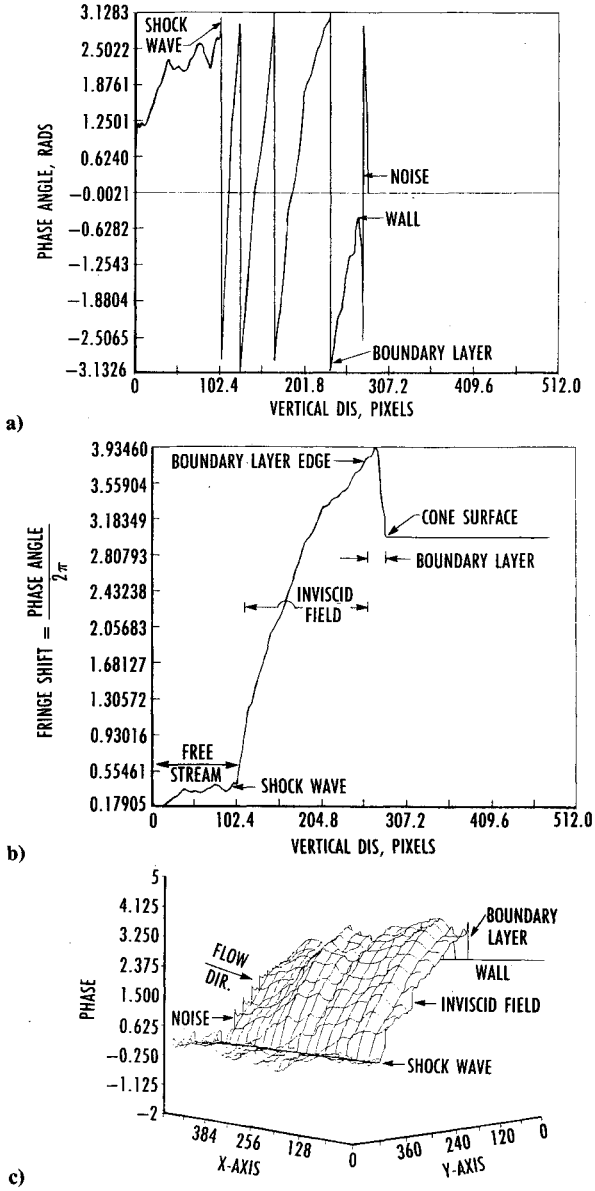

Fig. 8 Phase data reduced from interferogram shown in Fig. 7b: a) wrapped phase data, b) unwrapped phase data, and c) three-dimensional phase map for Fig. 7c.

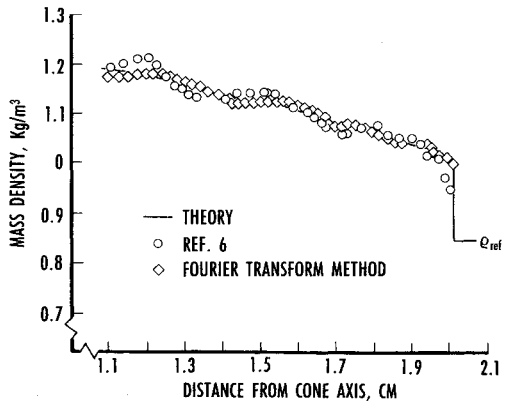

Fig. 9 Comparison between FTI reduce density and theory.

techniques. Using the 1000 line video camera, the data sampling increases to nominally 1×10^6 points, and recent advances in array processors and array cameras now allow for 16×10^6 points per interferogram! With data samplings of this size, statistical evaluations based on spatial distributions are obtainable, and if the randomness (turbulence) is statistically ergodic, some temporal characteristics of flow turbulence may be known because the spatial and temporal statistics are mathematically equivalent.

As an example, the interferogram in Fig. 7a can be reduced to radial flow densities, $\rho(\theta_c)$. For this axisymmetric flow, the inviscid fluid properties normalized by the freestream conditions are constant along rays emanating from the cone vertex. Thus $\bar{\rho}(\theta_c) = \mu_\rho(\theta_c)$, where $\mu_\rho(\theta_c)$ is the inviscid flow prediction for θ_c and $\bar{\rho}(\theta_c)$ is the average value of the measured flow densities along the ray corresponding to θ_c. The standard deviation associated with $\bar{\rho}(\theta_c)$ is proportional to the spatial structure of the flow turbulence, and the global structure of the density fluctuations can be studied by constructing a density perturbation map, each point given as $\rho_i'(\theta_c) = \rho_i(\theta_c) - \bar{\rho}(\theta_c)$ where i denotes a discrete value along the ray for θ_c. For an adiabatic flow, the velocity is given by the energy equation as

$$u_i^2 = 2C_p(T_0 - T_i) \tag{10}$$

Substituting $u_i(\theta_c) = \bar{u}(\theta_c) + u_i'(\theta_c)$ and $T_i(\theta_c) = \bar{T}(\theta_c) + T_i'(\theta_c)$ into Eq. (10) and rearranging terms leads to

$$[u_i'(\theta_c)]^2 + 2\bar{u}(\theta_c)u_i'(\theta_c) + 2\,C_p\,T_i'(\theta_c) = 0 \tag{11}$$

$$\bar{u}^2(\theta_c) = 2C_p[T_0 - \bar{T}(\theta_c)] \tag{12}$$

From the ideal gas equation of state,

$$T' = \frac{\rho'}{\bar{\rho} + \rho'}\,\bar{T} \tag{13}$$

assuming negligible pressure fluctuations. Thus,

$$[u_i'(\theta_c)]^2 + 2\,\bar{u}(\theta_c)u_i'(\theta_c) + 2C_p\,\bar{T}(\theta_c)\frac{\rho_i'(\theta_c)}{\rho(\theta_c)} = 0 \tag{14}$$

which for turbulent intensities less than 10% simplifies to

$$\frac{u_i'(\theta_c)}{\bar{u}(\theta_c)} \simeq \frac{2C_p\bar{T}(\theta_c)}{[\bar{u}(\theta_c)]^2}\,\frac{\rho_i'(\theta_c)}{\rho_i(\theta_c)} \tag{15}$$

By using inviscid flow predictions for pressure, $\bar{T}(\theta_c)$ is available from the equation of state, and $\bar{u}(\theta_c)$ is computed from Eq. (11). Equation (15) is used to compute a spatial turbulence intensity distribution and then the autocorrelation along the rays and the cross correlations from ray-to-ray are calculated and subsequently used to compute spatial length scales. Finally, by presuming the ergodic condition is valid, the turbulent intensity, length scales, and a one-dimensional Reynolds shear stress ($\rho' u'$ along θ_c) are known. Study is underway at AEDC to assess this hypothesis and the findings will be reported later.

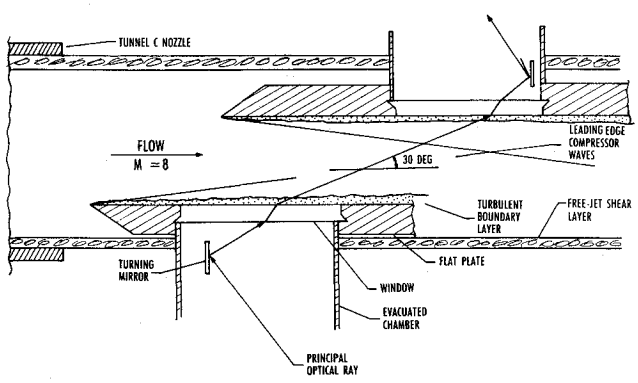

Fig. 10 Flush-mounted window flat plate beam transmission device.

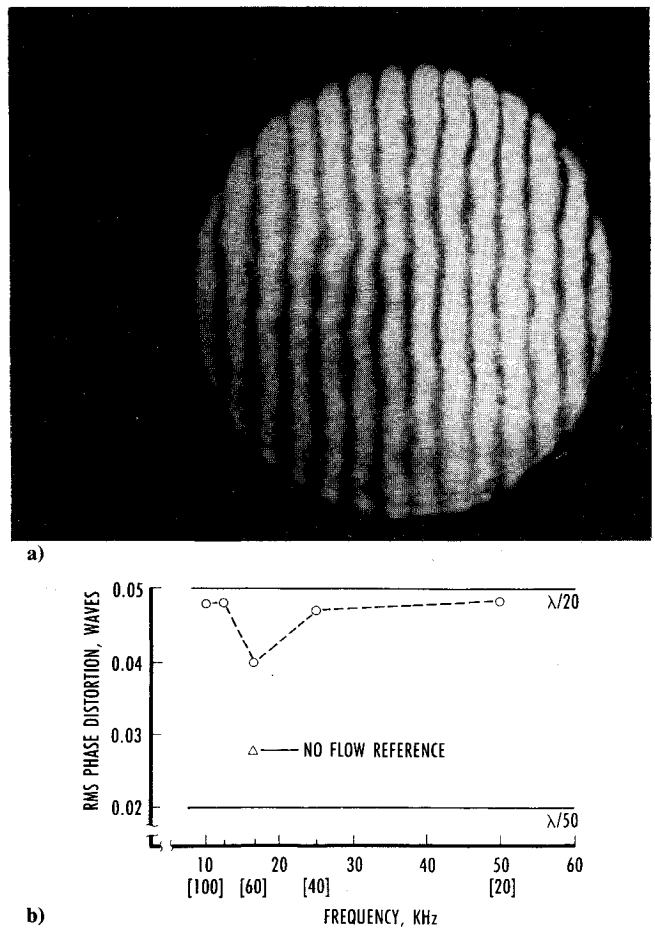

Fig. 11 Holographic interferometric measurements showing small aero-optic distortions for optical transmission scheme of Fig. 10: a) sample interferogram and b) rms phase distortion.

Aero-Optics Demonstration

Double-pulsed holographic interferograms of an aero-optics test performed in AEDC's hypersonic tunnel-C facility[14,15] are used to quantify optical distortions caused by flow turbulence. This test was done to determine the usefulness of a specially designed aero-optics measuring system; among many objectives, one involved quantifying the aero-optical distortion for optical waves transmitted into and through the central flow of tunnel C operating at Mach 8 with a stagnation pressure and temperature of 1900 psia and 1450°R, respectively.

An important design requirement in aero-optics ground testing involves placing undistorted optical waves in the core of the aerodynamic flow. The scheme designed for tunnel C is a flush-mounted window flat-plate device that protrudes through the nozzle freejet shear layer. The optical waves avoid exposure to the shear layer and enter the core flow by passing through an evacuated channel, reflecting off a beam steering mirror, and then passing through the flush-mounted window. The plate has a sharp leading edge and is aligned parallel to the freestream, so the flow over the surface, and thus the window, develops as a new two-dimensional turbulent boundary layer. The plate is wide, so edge effects are ignored. For applications testing, the optical waves in the core flow interact with the flow concomitant to the flight model, but for this test, a second flush-mounted window is used instead. In this manner, the optical distortions for the transmitting plate are nominally one-half the actual values measured. Figure 10 illustrates the scheme for a 30-deg look angle relative to the freestream.

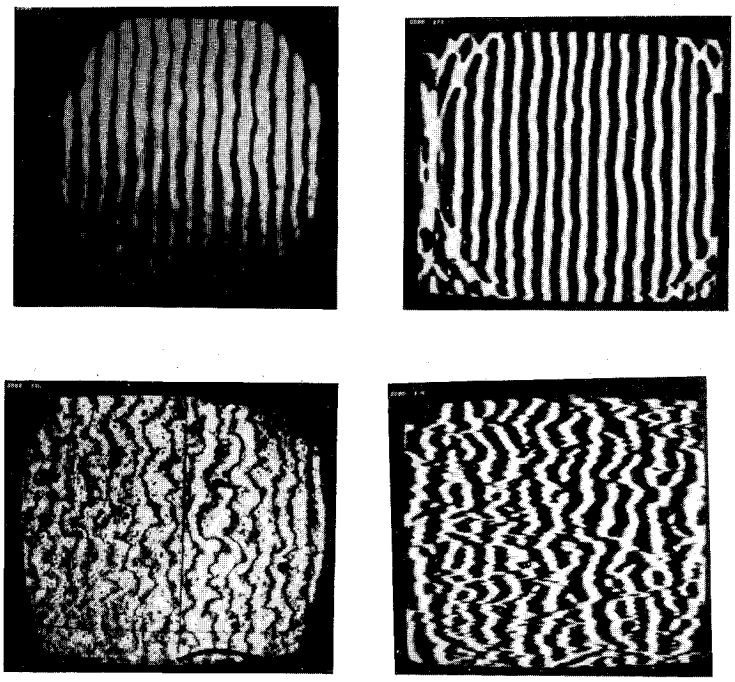

Fig. 12 Comparisons between real and phase-dependent interferograms: a) good agreement and b) poor agreement.

To assess the level of optical disturbance induced by the turbulence in the boundary-layer flow across the window, a series of double-pulsed holographic interferograms was obtained and analyzed using the AEDC FTI system. The purpose of the double-pulsed holographic interferometric measurements was to verify that the aerodynamic and high-frequency facility vibrations do not induce optical distortions exceeding a 20th of a wavelength in rms phase, peak-to-valley. Double-pulse holographic interferograms naturally filter high-frequency disturbances that are proportional to the reciprocal of the laser pulse separation intervals (e.g., disturbances less than 10 kHz are not seen in a 100-μs double-pulse holographic interferogram). A typical result is shown in Fig 11a; and Fig. 11b shows that nominally the rms phase distortion is $\lambda/20$ for both windows, so the distortion for the waves entering the core flow is about $\lambda/40$, well below the design goal. Using the large aperture approximation, the Strehl loss is about 2.5%. Strehl ratio defines the loss in optical intensity and is defined as the ratio of the peak intensity of the disturbed waves to that of undisturbed waves. For large aperture optical systems, optical diffraction regulates the distortions and the Strehl ratio is $\exp(-k^2\phi^2)$. Strehl loss is 1 − Strehl ratio expressed as a percentage.

Errors

FTI assumes $I(x)$ is infinite, so real interferograms containing fringe disruptions present sources for truncation errors. Fringe disruption is the termination of fringes that occurs at interferogram boundaries and also at the edges of silhouettes of solid objects in the optical path. Takeda et al.[4] reduced the truncation error by using a Hanning window.[16] Roddier and Roddier[11] used Gerchberg's algorithm,[25] which allows the true boundaries of real interferograms to be extended so that the otherwise troublesome boundary errors are displaced into the extended regions. Osten and Hofling[11] discuss yet another method wherein "synthetic interferograms" are used to cope with fringe disruption problems.

Despite the benefits and capabilities previously discussed, FTI is not foolproof. Some examples of success and failure are shown in Fig. 12; the real interferograms are on the left, the verification ones are on the right. The pair in Fig. 12a shows good agreement, which suggests $\phi(x, y)$ are correct, but the pair in Fig. 12b shows a horrible verification interferogram, which suggests f_c is incorrect. The primary sources for error are incorrect determination of f_c; aliasing, in which case f_{co} does not exist; disruption of fringe contours; off-axis tilt in the fringes, which means a residual f_c remains in $\phi(x, y)$; and inadequate phase unwrapping procedures.

Conclusions

Fourier transform interferometry is shown here to be a worthy and reliable process to use in automated reduction of aerodynamic and aero-optical interferograms provided the spatial carrier frequency is known and the modulation sidebands are distinct. Otherwise, these conditions being unfulfilled, another technique such as PSI must be used. Unlike PSI where a minimum of three separate interferograms must be resolved, only one interferogram is needed for FTI, and this makes it especially useful for reducing double-pulse holographic interferograms. FTI data reduction, data resolution, and data base capabilities far exceed the former fringe tracking methods, and the potential to acquire new information to include three-dimensional unsteady and reacting flows is now good. Extensions to three-dimensional tomographic studies are now practical, because proficient reduction of two-dimensional interferograms is a necessary first step in tomography. In summary, the Fourier transform method contributes directly to the study of fluid flows eliminating an age-old drawback of the flowfield interferometry; namely, it allows for efficient reduction of the interferometric measurements.

Acknowledgments

The U. S. Army Strategic Defense Command in Huntsville, Alabama, the U. S. Air Force at AEDC, and the Instrumentation Research Division at NASA Langley Research Center, Hampton, Virginia, are acknowledged for their support. L. Montgomery Smith of the University of Tennessee Space Institute (UTSI) is gratefully acknowledged for providing instruction, guidance, and the original FTI algorithm used at AEDC.

References

[1]Trolinger, J. D., "Laser Applications in Flow Diagnostics," AGARDograph 275, 1988.

[2]Dandliker, R., and Thalmann, R., "Heterdyne and Quasi-Heterodyne Holographic Interferometry," *Optical Engineering*, Vol. 24, March 1985, pp. 824–831.

[3]Lai, G., and Yatagal, T., "Generalized Phase-Shifting Interferometry," *Journal of the Optical Society of America*, Vol. 8, May 1961, pp. 822–827.

[4]Takeda, M., Hideki, I., and Kobaysahi, S., "Fourier Transform Method of Fringe Analysis For Computer-Based Topography And Interferometry," *Journal of the Optical Society of America*, Vol. 72, Jan. 1982, pp. 156–160.

[5]Macy, W. W., Jr., "Two-Dimensional Fringe-Pattern Analysis," *Applied Optics*, Vol. 23, Dec. 1983 pp. 3898–3901.

[6]Mertz, L., "Real-Time Fringe-Pattern Analysis," *Applied Optics*, Vol. 22, May 1983, pp. 1535–1539.

[7]Nugent, K. A., "Interferogram Analysis Using An Accurate Fully Automated Algorithm," *Applied Optics*, Vol. 24, Sept. 1985, pp. 3101–3105.

[8]Roddier, C., and Roddier, F., "Interferogram Analysis Using Fourier Transform Techniques," *Applied Optics*, Vol. 26, May 1987, pp. 1668–1673.

[9]Kim, W., and Hayes, M. H., "Phase Retrieval Using Two Fourier-Transform Intensities," *Journal of the Optical Society of America*, Vol. 7, March 1990, pp. 441–449.

[10]Roddier, F., and Roddier, C., "Wavefront Reconstruction Using Iterative Fourier Transforms," *Applied Optics*, Vol. 30, April 1991, pp. 1325–1327.

[11]Osten, W., and Hofling, R., "The Inverse Process in Automated Fringe Analysis—Problems and Approaches," *Proceedings of Hologram Interferometry and Speckle Metrology*, Society for Experimental Mechanics, Baltimore, MD, Nov. 1990.

[12]Havener, G., "Holographic Measurements of Transition and Turbulent Bursting in Supersonic Axisymmetric Boundary Layers," *AIAA Journal*, Vol. 26, No. 12, 1988, pp. 1467–1476.

[13]Havener, G., "Detection of Boundary Layer Transition Using Holography," *AIAA Journal*, Vol. 15, No. 4, 1977, pp. 592, 593.

[14]Crosswy, L., and Havener, G., "Aero-Optics Measurement System For The AEDC Aero-Optics Test Facility," Arnold Engineering Development Center, AEDC TR-90-20 (ADA232852), Arnold Air Force Base, TN, March 1991.

[15]Havener, G., and Stepanek, C., "Aero-Optics Testing Capabilities at AEDC," AIAA Paper 92-0760, Jan. 1992.

[16]Gonzalez, R. C., and Wintz, P., *Digital Image Processing*, 2nd ed., Addison-Wesley, Reading, MA, 1987, Chap. 3.

[17]Bone, D. J., Bachor, H. A., and Sandeman, R. J., "Fringe-Pattern Analysis Using A 2-D Fourier Transform," *Applied Optics*, Vol. 25, May 1986, pp. 1653–1660.

[18]Huntley, J. M., "Noise-Immune Phase Unwrapping Algorithm," *Applied Optics*, Vol. 28, Aug. 1989, pp. 3268–3270.

[19]Haniff, C. A., "Least-Squares Fourier Phase Estimation From The Modulo 2π Bispectrum Phase," *Journal of the Optical Society of America*, Vol. 8, Jan. 1991, pp. 134–140.

[20]Bone, D. J., "Fourier Fringe Analysis: The Two-Dimensional Phase Problem," *Applied Optics*, Vol. 30, Sept. 1991, pp. 3627–3632.

[21]Hamming, R. W., *Digital Filters*, Prentice-Hall, Englewood Cliffs, NJ, 1977.

[22]Smith, L. M., Keefer, D. R., and Sudharsanan, S. I., "Abel Inversion Using Transform Techniques," *Journal of Quantative Spectroscopy and Radiative Transfer*, Vol. 39, No. 5, 1988, pp. 367–373.

[23]Kalal, M., and Nugent, K. A., "Abel Inversion Using Fast Fourier Transforms," *Applied Optics*, Vol. 27, May 1988, pp. 1956.

[24]Tieng, S. M., and Lai, Z., "Temperature Measurement of Reacting Flowfield by Phase-Shifting Holographic Interferometry," *Journal of Thermophysics and Heat Transfer,* Vol. 6, No. 3, 1992, pp. 445–451.

[25]Gerchberg, R. W., "Super-Resolution Through Error Energy Reduction," *Optica Acta*, Vol. 21, No. 6, 1974, pp. 709.